Reaction Chemistry of Solid-State Pyridine Thin Films with Vapor Deposited Ag, Mg, and Al

ARTICLE *in* THE JOURNAL OF PHYSICAL CHEMISTRY C · MAY 2012

Impact Factor: 4.77 · DOI: 10.1021/jp300795c

2 AUTHORS:

Dallas Matz
The University of Arizona
10 PUBLICATIONS **21** CITATIONS
SEE PROFILE

Jeanne E Pemberton
The University of Arizona
175 PUBLICATIONS **4,737** CITATIONS
SEE PROFILE

THE JOURNAL OF PHYSICAL CHEMISTRY C

Article

pubs.acs.org/JPCC

Reaction Chemistry of Solid-State Pyridine Thin Films with Vapor Deposited Ag, Mg, and Al

Dallas L. Matz and Jeanne E. Pemberton*

Department of Chemistry and Biochemistry, University of Arizona, 1306 East University Boulevard, Tucson, Arizona 85721, United States

ABSTRACT: The reaction of pyridine in thin solid-state films with post-deposited Ag, Mg, and Al is investigated using surface Raman spectroscopy in ultrahigh vacuum. Vapor-deposited Ag forms metallic nanoparticles on the pyridine film, resulting in surface enhancement of the Raman scattering (SERS), with no reaction chemistry evident. Mg and Al react with pyridine by electron transfer to form radical anion intermediates, some of which are stabilized by entrapment in the solid pyridine matrix. With Mg, slight SERS enhancement is observed along with Mg-to-pyridine electron transfer to form pyridyl radical anions, some of which dimerize to 4,4′-bipyridine with loss of MgH_2 and a neutral Mg atom. With Al, the reaction chemistry is initiated by a similar Al-to-pyridine electron transfer, but the radical anions so formed undergo further degradation to amorphous carbon. In total, these results demonstrate the complex reaction chemistry that can occur between heterocycles in the solid state and low work function metal atoms.

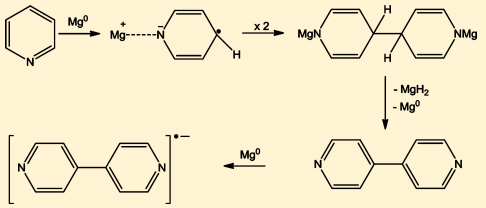

INTRODUCTION

The chemistry of aromatic heterocycles with reactive metals such as Ag, Mg, and Al as atoms, ions, colloids, and in the bulk has been of interest in many scientific disciplines including surface chemistry,[1] organometallic chemistry,[2−4] environmental science,[5] interstellar chemistry,[6] and biological systems.[7−12] The simplest and best understood aromatic heterocyclic system is pyridine. To date, most studies of the chemistry between pyridine and reactive metals such as Ag, Mg, and Al have been performed on single pyridine molecules with metal atoms or cations in the gas[10,11,13−19] or solution phases,[20] or in theoretical studies for pyridine in similar limited environments.[4,13,16,19,21−23] Although previous work has provided considerable insight into this area, comparably little is known about the reaction chemistry of solid-state pyridine films with such metals. The reaction chemistry of solid-state heterocyclic systems with reactive metals has recently emerged as an important consideration for the continued development of organic semiconductor materials used in organic electronics, solid-state synthesis,[24] and niche biological applications.[25] Despite this increasing importance, limited work has been reported to elucidate the reaction chemistry between solid-state heterocyclic aromatics and reactive metals.[26]

The Ag-pyridine system has been studied extensively in gas[14,16,17] and solution[20] phases, in theoretical work,[16,21−23] and in the surface-adsorbed state, especially in studies using surface enhanced Raman scattering (SERS).[22,27−34] The chemistry between Mg and pyridine is also well-developed in the gas[10,11,13,15,18] and solution[20] phases and by theory.[13,19] For Mg, these studies have focused predominantly on interactions occurring in isolated 1:1 Mg^+:pyridine conjugates, although one study of co-condensed Mg and pyridine was reported in which bipyridyl was identified as a reaction product.[35] The reaction chemistry between Al and pyridine has been given the least attention to date, with only one gas phase[11] and one theoretical[4] study of Al^+-pyridine conjugates reported.

On the basis of the limited information available about the solid-state chemistry of pyridine with Al and Ag and the single but intriguing report for the Mg-pyridine system in the solid state, it is of interest to further investigate these systems. Toward that end, surface Raman spectroscopy is used here to explore these systems in ultrahigh vacuum with the goal of elucidating any commonality in reaction pathway among the three systems. Our specific interest in these systems is motivated by the need to better understand the interfacial chemistry that governs charge injection efficiency at metal−organic heterojunctions in organic electronic devices, such as organic light emitting diodes, organic photovoltaics, and organic field effect transistors.[36−40] Low work function metals are commonly used as contacts in these devices to minimize the charge injection or charge harvesting barrier between the organic semiconductor and the metallic contact.[38,41]

Previous investigations in this laboratory on the interfacial chemistry of the organic semiconductor tris(8-hyroxyquinoline) aluminum (Alq_3) with Ag,[42] Mg,[43] and Al,[42] of *trans*-stilbene with Al,[44] and of benzene with Ag, Mg, and Al[26] have been reported. The spectral data generated in these studies has documented the unanticipated complexity of the reaction chemistry possible, even with simple systems. The work reported here extends these studies to the simplest organic aromatic compound containing a N-heteroatom, pyridine, in an attempt to better define molecular variables influencing reaction chemistry pathways. N-containing heterocycles are constituent components of multiple organic semiconductor

Received: January 24, 2012
Revised: April 4, 2012
Published: April 25, 2012

   dx.doi.org/10.1021/jp300795c | *J. Phys. Chem. C* 2012, 116, 11548−11555

systems such as Alq_3, etc., thereby justifying its choice as a model organic compound. Its reaction chemistry in the initial stages of ohmic contact formation with Ag, Mg, and Al post-deposited in the vapor phase is presented here.

EXPERIMENTAL SECTION

Materials. All experiments were performed on substrates of 1.25 cm diameter polycrystalline Ag (99.999%, Alfa Aesar). Pyridine (≥99.9%, Chromasolv Plus HPLC grade) and 4,4′-bipyridine (98%) were purchased from Sigma-Aldrich. Sources of metal were Al wire (99.999%, Sigma-Aldrich), Ag foil (99.9%, Sigma-Alrich), and Mg turnings (99.98% under Ar, Alfa Aesar). H_2SO_4 (EMD, 98%), $HClO_4$ (EMD, 70%), HCl (EMD, 37%), CrO_3 (Alfa Aesar, 98+%), and NH_4OH (EMD, 28−30%) were used in the chemical polishing of Ag substrates. Purified water (>18 MΩ resistivity and <8 ppb organic content) was obtained using a Waters Milli-Q UV Plus purification system (Millipore Corp.) All materials were used as received unless noted otherwise.

Ultrahigh Vacuum Chamber. Thin films of pyridine and metal (Ag, Al, and Mg) were deposited and subsequently characterized in a custom-built UHV chamber described previously.[42−44] This system consists of three chambers: a load-lock sample entry chamber maintained at $\sim 5 \times 10^{-7}$ Torr, a sample preparation chamber maintained at $< 5 \times 10^{-10}$ Torr, and an analysis chamber maintained at $< 5 \times 10^{-11}$ Torr. The sample preparation chamber was never allowed to achieve pressures above 10^{-9} Torr during sample preparation and subsequent handling.

Surface Preparation and Thin Film Deposition. Prior to introduction into the UHV chamber, Ag substrates were mechanically and chemically cleaned[45] and polished to rms roughness of ∼1 nm by AFM[46] according to procedures described previously.[46,47] Surfaces so prepared were placed into stainless steel holders and inserted into the vacuum chamber. Once at base pressure, the substrates were cooled to ∼30 K on a custom-built, translatable cryoarm (DE-204B, Advanced Research System) using a closed-loop He compressor cryostat (HC-4, APD Cryogenics). Temperatures near the surface were measured using a type K thermocouple and regulated with a cryogenic temperature controller (Cryo-Con Model 34).

Solid-state pyridine thin films were vapor deposited through a glass capillary array;[48] dissolved gases in the pyridine were first removed with three freeze−pump−thaw cycles prior to deposition. Film thicknesses, reported in uncorrected Langmuirs (L),[49] were deposited at a rate of 0.3 L/s with an assumed sticking coefficient of unity, equating to $\sim 1.5 \times 10^{15}$ pyridine molecules/cm^2.[33] Metal films were deposited from Al_2O_3-coated Ta boats (ME9-A0-M0-M5, R. D. Mathis Co.) and monitored using a quartz crystal microbalance and thickness monitor (model TM-400, Maxtek Inc.) cooled to liquid N_2 temperatures. Reaction chemistry is monitored by comparing the spectra of pristine pyridine films to those observed after deposition of metal in 5 Å increments (equivalent to $\sim 2.0 \times 10^{15}$ atoms/cm^2 of Ag and Al and $\sim 1.4 \times 10^{15}$ atoms/cm^2 of Mg assuming bulk metal densities) up to 20 Å in mass thickness.

Raman Spectroscopy. Raman spectra were collected using a previously described optical arrangement[43] with a 532 nm Nd:YVO_4 diode laser (Coherent Verdi 2W) and a Newton EM-CCD (Andor Technology DU971P-BV). Spectra were collected using 10 min acquisition times, 30 mW laser power at the surface, and a spectral bandpass of 5 cm^{-1}.

Peak fitting was performed using 100% Gaussian peak shapes. Peak frequencies for pyridine were fit using values (±5 cm^{-1}) obtained from Moskovits et al.[32] with full width at half-maximum (fwhm) values of 15 ± 10 cm^{-1} and relative intensities ±20%. Additional graphitic carbon modes were fit using five broad bands with peak frequencies (±20 cm^{-1}), fwhm, and relative intensities (±50%) from Ferrari and Robertson.[50,51] Fits were deemed acceptable when the χ^2 values exceeded 0.99.[52]

RESULTS AND DISCUSSION

Raman spectra between 200 and 2100 cm^{-1} from 5-L solid-state, pyridine films are shown as black lines in Figures 1, 3, and

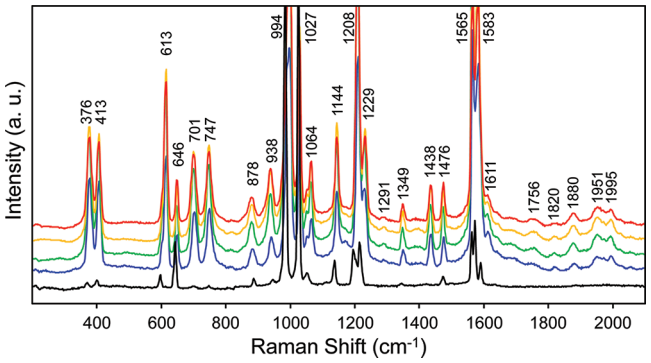

Figure 1. Raman spectra of a pristine 5-L pyridine film at 30 K (black) and post deposition of 5 (blue), 10 (green), 15 (gold), and 20 (red) Å of Ag.

6.[32] It has been shown previously that, under deposition parameters similar to those used here, pyridine forms amorphous solid-state films.[18] Nineteen bands can be distinguished in these spectra that are attributable to the Raman-active normal modes of pyridine, along with one combination band. Peak frequencies and assignments are given in Table 1.

Metallization with Ag. Raman spectra of 5-L pyridine thin films subjected to sequential 5 Å mass thickness depositions of Ag from the vapor phase are shown in Figure 1; spectral bands and assignments are given in Table 1. Upon deposition of Ag, an increase in intensity of all pyridine Raman bands is observed with six bands, ν_1, ν_3, ν_{6a}, ν_{8a}, ν_{9a}, and ν_{10b}, exhibiting significant (>10 cm^{-1}) frequency shifts. Two pyridine normal modes appear at 1064 and 1438 cm^{-1} that are too weak to be observed in the spectrum of the pristine pyridine film prior to Ag deposition. In addition, pyridine combination and overtone bands at 1291, 1689, 1756, 1820, 1880, 1951, and 1995 cm^{-1} are also observed upon Ag deposition.[32,53] Beyond these intensity changes of the pyridine normal modes, no new bands attributable to any reaction chemistry are observed.

Figure 2 shows the Raman intensities for a select series of pyridine bands as a function of Ag coverage normalized to the intensity of the ν_1 band at 994 cm^{-1}. All of these bands experience surface enhancement of their Raman scattering (SERS), presumably from the formation of Ag nanoparticles on the surface, as indicated by the intensity increase that occurs for deposition of the first 5 Å of Ag. The intensity of these bands decreases slightly beyond this Ag coverage as the pyridine film becomes increasingly metallized and opaque up to 20 Å of Ag; beyond this coverage (spectra not shown), the intensities of pyridine decrease drastically as metallization becomes complete.

dx.doi.org/10.1021/jp300795c | J. Phys. Chem. C 2012, 116, 11548−11555

Table 1. Raman Peak Frequencies and Assignments for a 5-L Solid-State Pyridine Film before and after Ag Deposition

frequency (cm^{-1})		assignments[a]	
pristine film	post Ag deposition (cm^{-1} shift)	Wilson no.	mode
372	376 (4)	ν_{16a}	$\delta(\text{ring})_{oop}$
406	413 (7)	ν_{16b}	$\delta(\text{ring})_{oop}$
599	613 (14)	ν_{6a}	$\delta(\text{ring})_{ip}$
645	646 (1)	ν_{6b}	$\delta(\text{ring})_{ip}$
703	701 (−2)	ν_{11}	$\delta(\text{C–H})_{oop}$
751	747 (−4)	ν_{4}	$\delta(\text{ring})_{oop}$
884	878 (−6)	ν_{10a}	$\delta(\text{C–C})_{oop}$
947	938 (−9)	ν_{10b}	$\delta(\text{C–H})_{oop}$
984	994 (10)	ν_{1}	sym ring breathing (ip)
1027	1027 (0)	ν_{12}	trig ring breathing (ip)
1055	1051 (−4)	ν_{18a}	$\delta(\text{C–H})_{ip}$
	1064	ν_{18b}	$\delta(\text{C–H})_{ip}$
1140	1144 (4)	ν_{15}	
1197	1208 (11)	ν_{9a}	$\nu(\text{ring})_{ip}$
1218	1229 (11)	ν_{3}	$\delta(\text{C–H})_{ip}$
	1291	$2 \times \nu_{6b}$	
1347	1349 (2)	ν_{14}	$\delta(\text{C–H})_{ip}$
	1438	ν_{19b}	$\delta(\text{C–H})_{ip}$
1477	1476 (−1)	ν_{19a}	$\delta(\text{C–H})_{ip}$
1566	1565 (−1)	ν_{8b}	$\nu(\text{ring})_{ip}$
1572	1583 (11)	ν_{8a}	$\nu(\text{ring})_{ip}$
1591	1611 (20)	$\nu_{1} + \nu_{6a}$	
	1689	$\nu_{1} + \nu_{11}$	
	1756	$\nu_{1} + \nu_{4}$	
	1820	$\nu_{10a} + \nu_{10b}$	
	1880	$2 \times \nu_{10b}$	
	1951	$2 \times \nu_{1}$	
	1995	$\nu_{1} + \nu_{12}$	

[a]Assignments taken from refs 32 and 54.

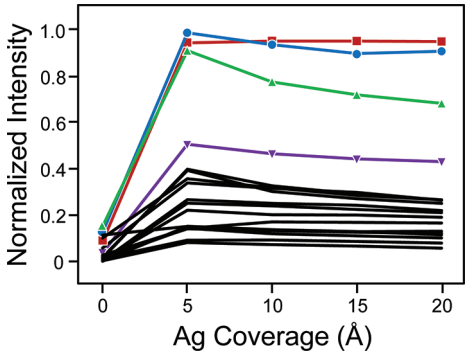

Figure 2. Normalized Raman intensities as a function of Ag coverage for pyridine bands: ν_{6a} (purple ▼), ν_{8a} (green ▲), ν_{8b} (blue ●), and ν_{9a} (red ■); all other major pyridine modes are plotted as black lines with no markers.

The greatest SERS enhancements are observed for the ν_{6a}, ν_{9a}, ν_{8a}, and ν_{8b} modes of pyridine, which is consistent with previous SERS observations for pyridine on Ag. Moskovits et al.[32] and Arenas et al.[27] previously attributed preferential enhancement of the ν_{6a}, ν_{9a}, and ν_{8a} modes to charge transfer chemical enhancement contributions to SERS from pyridine chemisorption to the Ag surface. In addition, Vivoni et al.[54] predicted shifts of $\geq$10 cm^{-1} to higher frequency for the ν_{1}, ν_{3}, ν_{6a}, ν_{8a}, ν_{10b}, and ν_{18b} pyridine modes in calculations of the Raman spectral behavior for pyridine chemisorbed on Ag. These predicted shifts are similar to those observed here with two exceptions. Although their calculations predict a 1 cm^{-1} shift for ν_{9a}, a shift of 11 cm^{-1} is actually observed, as shown in Figure 1. They also predict a shift of 16 cm^{-1} for ν_{18b} that cannot be observed in our experiments due to the absence of this band in the spectrum of the pristine film. Collectively, these frequency shifts were attributed to a weak chemisorption interaction between the pyridine N atom and the Ag surface with the ring perpendicular to the surface. It was further predicted that a flat ring orientation would actually result in shifts to lower frequency due to back-donation of electron density from the surface to pyridine π^* levels.[55,56]

DFT calculations of pyridine adsorbed on Ag(110) performed by Hahn et al.[21] suggest that pyridine–Ag bonding involves a partial electron donation from the N atom lone pair electrons to the Ag 5s orbital with a larger contribution from back-donation from the Ag d_z^2 to the N p_z level resulting in a weak σ-bond, a slight negative charge on the N atom, and a binding energy of ~23 kcal/mol. Values for the ν(Ag–N) mode have been reported anywhere from 173 to 240 cm^{-1};[29,34,54] unfortunately, this range spans the low frequency cutoff (~200 cm^{-1}) of the holographic notch filter used here to eliminate Rayleigh scattered radiation, thereby prohibiting acquisition of reliable spectral information in this region.

The observation of increased normal mode intensities and combination/overtone modes is characteristic of SERS and consistent with what has been observed previously.[22,27,31,32,34,54,57] In total, these results are consistent with a picture in which small nanoparticles of Ag form either on the film surface or in the near-surface region of the solid-state pyridine film during deposition, causing subsequent rearrangement of the nearby pyridine molecules to facilitate interaction with the Ag through the N lone pair electrons. This chemisorption interaction leads to the spectral shifts and slight preferential spectral band enhancements observed. Beyond these relatively minimal effects, no further reaction chemistry occurs. Finally, in contrast to previous UHV Raman studies on pyridine on roughened Ag surfaces with excitation in the range 350–410 nm by Goncher et al.,[58] no evidence of photochemically initiated degradation chemistry is observed in the work reported here. Although detailed excitation studies are beyond the scope of this work, we presume that the absence of any photochemical reaction chemistry is due to the much lower energy (532 nm, 2.3 eV) used to excite Raman scattering and the use of chemically polished, smooth Ag substrates.

Metallization with Mg. Raman spectra from the progressive metallization of a pyridine film with Mg are shown in Figure 3; peak frequencies and assignments are given in Table 2. All of the pyridine normal modes of the pristine film are still distinguishable and considerably enhanced in intensity in the spectra upon metallization (e.g., ν_{16a}, ν_{6b}, ν_{1}, ν_{12}, ν_{9a}, and ν_{8b}); this enhancement is attributed to SERS from Mg nanoparticles, consistent with previous observations.[59,60] Additionally, several new bands are observed that suggest reaction chemistry. These new bands include those at 276, 334, 475, 522, 599, 659, 813, 1041, 1187, 1240, 1274, 1400, 1500, and 1531 cm^{-1} that gradually increase in intensity with Mg coverage and those at 544, 690,793, 879, 937, and 1626 cm^{-1} that appear initially upon Mg deposition but diminish in intensity with higher Mg coverage. The ν_{1}, ν_{3}, ν_{6a}, ν_{8a}, ν_{10b}, and ν_{18b} bands show significant shifts to higher frequency similar to those noted above for Ag. In the region between 1800 and 2100 cm^{-1}, several weak combination and overtone bands are also

dx.doi.org/10.1021/jp300795c | J. Phys. Chem. C 2012, 116, 11548–11555

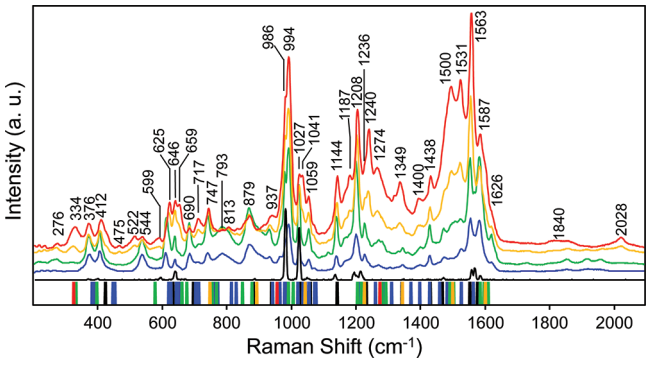

Figure 3. Raman spectra of a pristine 5-L pyridine film at 30 K (black) and post deposition of 5 (blue), 10 (green), 15 (gold), and 20 (red) Å of Mg. Tick marks beneath the spectra identify characteristic frequencies for pyridine (black), *p*-pyridyl radical anion (blue), 4,4′-bipyridine (green), 4,4′-bipyridyl radical anion (gold), and MgH_2 (red).

observed. In the region between 1100 and 1600 cm^{-1}, these new bands are superimposed on a background of two broad bands centered near 1300 and 1530 cm^{-1}. To aid in discussion of the spectral interpretation, previously observed or predicted frequencies for proposed species are indicated by color-coded tick marks below the spectra in Figure 3.

Strong evidence for the presence of the *p*-pyridyl radical anions in these films is provided by the new bands at 544, 690, 793, and 1400 cm^{-1}.[61,62] In addition to these discrete bands, additional bands at 376, 625, 646, 986, 1041, 1236, and 1531 cm^{-1} are partially assigned to the *p*-pyridyl radical anion. These latter modes are more difficult to definitively assign to the pyridyl radical anion due to spectral overlap with the bands of pyridine. The frequencies for the new bands assigned to the *p*-pyridyl radical anion are in close agreement with those calculated by LaVerne et al.[62] and Cheng et al.,[61] as given in Table 2.

The radical anion species are proposed to be created through electron transfer from Mg to pyridine. This chemistry is similar to that recently reported by this laboratory for metallization of thin solid-state films of benzene with Mg.[26] Such electron transfer would at first glance seem unlikely given that the adiabatic electron affinity (AEA) for an isolated, gas-phase pyridine molecule is −0.62 eV.[63] This negative value implies instability of the pyridyl radical anion, making metal-to-pyridine charge transfer appear improbable. However, it has been demonstrated by Han et al.[64] using photoelectron spectroscopy that the AEA for pyridine clusters changes as a function of cluster size, with the AEA for a 13 pyridine cluster increasing to 1.02 eV. Self-solvation of the anion in pyridine clusters must provide stabilization that is not possible with isolated molecules, thereby allowing metal-to-pyridine charge transfer to readily occur in environments such as the thin films being investigated here.

Precedent for this pathway does exist in the literature. Solution-phase studies of pyridine with Na[65] and Li[66] and condensed phase studies of pyridine with Ca, Li, and Mg[35] using ESR[65,67] and NMR[65] spectroscopy suggest reaction through a metal-catalyzed oxidative dimerization pathway via a radical anion intermediate. On this basis, the initial step in the pathway shown in Figure 4 that is proposed to explain the results for the solid-state pyridine films studied here involves a one-electron transfer from Mg to the pyridine ring, producing a radical anion.[66] Specifically, the *p*-pyridyl radical anion is proposed to form almost exclusively due to the larger δ^+ residing on the C atom in the para position, having the greatest spatial separation from the negative charge on the electronegative N atom, where a majority of the electron density resides.[67,68] This radical anion species is further stabilized by weak association of the negative charge on the N atom with the Mg^+ so created. Two radical anions then couple to form a reduced dimer, which can then undergo hydride transfer to form MgH_2,[66] releasing the second Mg as a neutral atom. This dimerization is proposed to occur quickly in the solid state due to the proximity of the Mg^+−*p*-pyridyl anion radical pairs.[65] Although no specific vibrational band is observed for the Mg−N bond due to the low frequency cut-off of our holographic notch filters, the shifts observed in the ν_1, ν_3, ν_{6a}, ν_{8a}, ν_{10b}, and ν_{18b} bands are consistent with *ab initio* calculations by Vivoni et al.[54] that support this pathway.

The bands observed at 334, 522, 747, 994, 1041, 1236, 1240, 1349, 1400, 1500, 1531, and 1587 cm^{-1} are assigned to 4,4′-bipyridine based on Raman assignments for this molecule in the solution phase,[69] in theoretical studies,[70,71] and in surface studies on Ag, Au, Rh, and Zn.[72−76] Figure 5 shows a comparison between the spectrum of the solid-state pyridine film after deposition of 20 Å of Mg and the spectrum of 4,4′-bypyridine. Lu et al.[75] have shown that the relative intensities and peak frequencies of the 4,4′-bypyridine bands are highly sensitive to the local environment of the molecule, in particular its redox state. The positive electron affinity of 4,4′-bipyridine of ∼1 eV,[51] compared to that for pyridine of −0.62 eV,[63] translates to a more easily reduced species. Given the higher electron affinity of bipyridine than pyridine, it is reasonable to expect that bipyridine, once formed, can be reduced upon subsequent Mg deposition to form the corresponding anion radical. Alternately, Jagur-Grodzinski has postulated the reduction of bipyridine by the pyridyl anion radical.[65] Thus, the possibility exists that three forms of bipyridine are present: neutral, radical anion, and/or dimerized complex with Mg. All of these species would contribute to the observed spectra affecting the apparent relative intensities of the bipyridine contributions as well as the peak frequencies. Moreover, in solution SERS experiments on 4,4′-bipyridine on Ag, Strekas[76] observed that the 1626 cm^{-1} band lost almost all intensity, while the bands at 1516 and 1219 cm^{-1} become greatly enhanced. Another factor in band assignments is the extent to which the frequencies are influenced by interaction of the 4,4′-bipyridine with the surface of Mg nanoparticles. Gu et al.[72] have shown that many of the 4,4′-bipyridine frequencies shift by as much as 30 cm^{-1} when interacting with metals such as Zn, Rh, and Au, and they also report a variance in relative intensities similar to that observed by Strekas.

Figure 6 is a plot of normalized intensity of select pyridine and reaction product bands as a function of Mg coverage; all bands have been normalized to the highest intensity of that band in the series of spectra shown in Figure 3. Six modes were selected for presentation in Figure 5 based on their freedom from spectral interference. Results are shown for the neat pyridine band at 1027 cm^{-1}, the 4,4′-bipyridine bands at 334 and 1500 cm^{-1}, and the *p*-pyridyl radical anion bands at 544 and 793 cm^{-1}. The neat pyridine band increases in intensity due to the SERS effect until a Mg coverage of 10 Å, after which the intensity decreases, consistent with its consumption to form products. The *p*-pyridyl radical anion bands initially grow in intensity but then decrease at Mg coverage >10 Å as the 4,4′-

dx.doi.org/10.1021/jp300795c | J. Phys. Chem. C 2012, 116, 11548−11555

Table 2. Raman Peak Frequencies and Assignments for a 5-L Solid-State Pyridine Film before and after Mg Deposition

	pyridine		*p*-pyridyl radical anion			4,4′-bipyridine (BiPy)		$BiPy^{\bullet-}$	MgH_2
observed frequency	frequency (Wilson no.)[a]	assignments[b]	frequency[c,d]		assignments[d]	frequency (Ag SERS)[e]	assignments[f]	frequency[g]	frequency[h]
276						231			
334						352			312
376	376 (ν_{16a})	$\delta(\text{ring})_{oop}$	370	377	$\delta(\text{mol})_{oop}$	386			
412	412 (ν_{16b})	$\delta(\text{ring})_{oop}$							
475			436	442	$\delta(\text{mol})_{oop}$				
525									
544						568	δ(ring)		
599									
625	625 (ν_{6a})	$\delta(\text{ring})_{ip}$	612	619	$\delta(\text{mol})_{ip}$	624	$\delta(\text{ring})_{ip}$		
646	646 (ν_{6b})	$\delta(\text{ring})_{ip}$	636	644	δ(mol)				
659						655	$\delta(\text{ring})_{oop}$		
690	690 (ν_{11})	$\delta(\text{C–H})_{oop}$	697						
717				707	δ(ring)				
747	747 (ν_4)	$\delta(\text{ring})_{oop}$	754			768	$\delta(\text{ring})_{ip}$	742	
793				767	$\delta(\text{C–H})_{oop}$				
813			810	825	$\delta(\text{H–C–C–H})_{oop}$				
879	879 (ν_{10a})	$\delta(\text{C–H})_{oop}$				857	$\delta(\text{C–H})_{oop}$ $\delta(\text{ring})_{oop}$		
937	937 (ν_{10b})	$\delta(\text{C–H})_{oop}$	940	956	$\delta(\text{H-CCC-H})_{oop}$				954
986	986 (ν_1)	$\delta(\text{C–H})_{ring}$	961	978	δ(C–H)				
994			963	981	$\delta(\text{N–C–C–C})_{ip}$			990	
1027	1027 (ν_{12})	$\delta(\text{C–H})_{ring}$	1020			1014	$\delta(\text{ring})_{ip}$		
1040	1040 (ν_{18b})	$\delta(\text{C–H})_{ip}$	1045	1036	δ(ring)			1043	
1059	1059 (ν_{18a})	$\delta(\text{C–H})_{ip}$	1056	1073	δ(H)	1076	$\delta(\text{ring})_{ip}$ ν(C–N)		
1144	1144 (ν_{15})			1077	δ(H-CCC-H)				
1187									
1208	1208 (ν_{9a})	$\nu(\text{ring})_{ip}$	1209						
1236	1236 (ν_3)	$\delta(\text{C–H})_{ip}$	1217	1228	δ(H-CCC-H)	1232	$\delta(\text{ring})_{ip}$	1230	
1240				1265	$\delta(\text{ring})_{ip}$				
1274			1291			1292	$\delta(\text{ring})_{ip}$		1279
1349	1349 (ν_{14})	$\delta(\text{C–H})_{ip}$	1377	1316	$\delta(\text{H})_{ip}$			1350	
1403				1405	$\delta(\text{H-CNC-H})_{ip}$				
1438	1438 (ν_{19b})	$\delta(\text{C–H})_{ip}$	1436	1468	δ(H-CCC-H)				
1500	1476 (ν_{19a})	$\delta(\text{C–H})_{ip}$	1491					1509	
1528				1536	ν(C–N–C)	1512	ν(C–N) $\delta(\text{C–H})_{ip}$		
1563	1563 (ν_{8b})	$\nu(\text{ring})_{ip}$							
1587	1587 (ν_{8a})	$\nu(\text{ring})_{ip}$	1574			1608	ν(C–C)		
1626				1615	ν(ring)	1626	ν(ring)	1612	

[a]Assignments taken from ref 32. [b]Assignments taken from ref 54. [c]Assignments taken from ref 62. [d]Assignments taken from ref 61. [e]Assignments taken from ref 74. [f]Assignments taken from ref 69. [g]Assignments taken from ref 82. [h]Assignments taken from ref 83.

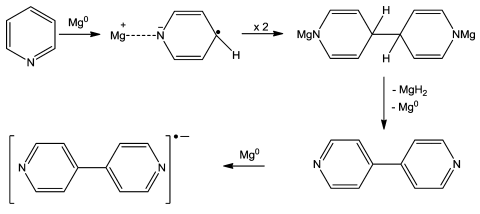

Figure 4. Proposed pathway for the reaction of Mg with pyridine.

bipyridyl bands emerge. Additionally, the band observed at 1274 cm^{-1} corresponds to MgH_2[77] and grows in at a rate similar to that of the 4,4′-bipyridine bands. These trends are consistent with the mechanism proposed in Figure 4, which shows that, as the pyridine film is metallized by Mg, *p*-pyridyl radical anions are formed initially and subsequently dimerize.

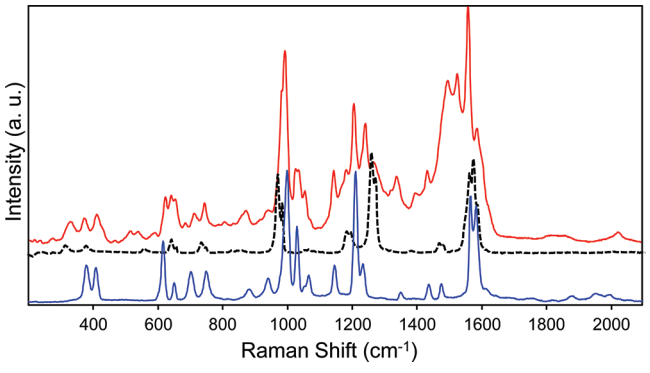

Figure 5. Raman spectra of a 5-L pyridine film at 30 K and post deposition of 20 Å of Mg (red) and 20 Å Ag (blue); a Raman spectrum from bulk 4,4′-bipyridine (black dash) is added for reference.

dx.doi.org/10.1021/jp300795c | J. Phys. Chem. C 2012, 116, 11548–11555

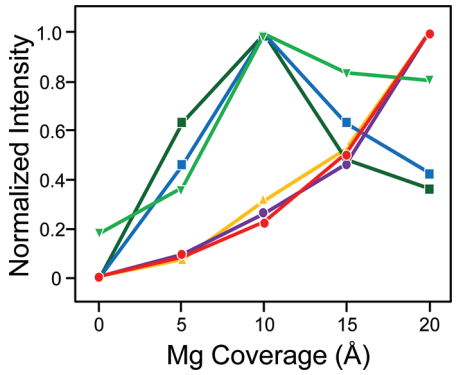

Figure 6. Normalized Raman intensities as a function of Mg coverage for the pyridine band at 1027 cm^{-1} (green ▼), the pyridyl radical bands at 544 cm^{-1} (green ■) and 793 cm^{-1} (blue ■), the 4,4′-bipyridine bands at 334 cm^{-1} (purple ●) and 1500 cm^{-1} (red ●), and the MgH_2 band at 1274 cm^{-1} (yellw ▲).

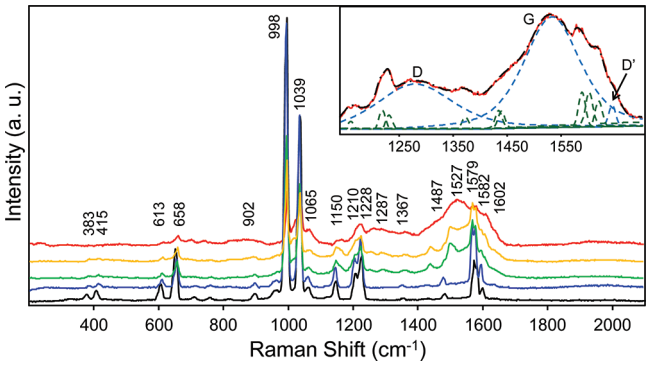

Figure 7. Raman spectra of a pristine 5-L pyridine film at 30 K (black) and post deposition of 5 (blue), 10 (green), 15 (gold), and 20 (red) Å of Al. The inset is the spectral fitting result for amorphous carbon with the original Raman spectrum (red —), the overall fit envelope (black – · –), the normal pyridine modes (green - - -), and the amorphous carbon modes (blue - - -).

This dimerization consumes the radical anions to produce bipyridine, MgH_2, and a neutral Mg atom. Due to spectral overlap of the bipyridine and bipyridine radical anion vibrational bands, no distinction can be made for this plot; it is likely that the observed intensities reflect the sum of the neutral and radical anion bipyridine species.

Evidence for the formation of small amounts of amorphous carbon is also apparent in the spectra in the form of the two broad bands that emerge with increasing Mg coverage, one between ∼1100 and 1400 cm^{-1} and the second between ∼1400 and 1600 cm^{-1}. Insight into the possible source of this amorphous carbon comes from theoretical studies by Liu et al.[78] and Cheng et al.[61] in which *p*-pyridyl radical anion decomposition via a ring-opening pathway is documented. Both studies predict required energies on the order of ∼2.5−3.0 eV to break either a C−C or C−N bond of a pyridyl radical anion, resulting in an open-chain radical species. We hypothesize that these degradation products further react and decompose into amorphous carbon, which is known to exhibit intense, broad Raman bands centered near ∼1250 and 1500 cm^{-1}.[50] Although no direct spectral evidence for such intermediates can be identified in these complex spectra, likely due to their relatively low abundance, the resulting amorphous carbon has a very large Raman scattering cross section, requiring very little of it to be present to be spectrally detected. The close overlap of many of the vibrational bands of pyridine, the *p*-pyridyl radical anion, 4,4′-bipyridine, and the 4,4′-bipyridyl anion radical, along with the suspected presence of amorphous carbon, makes reliable spectral decomposition of these congested spectra virtually impossible.

Metallization with Al. Figure 7 shows Raman spectra of a solid-state pyridine film upon progressive metallization with Al; peak frequencies and assignments are given in Table 3. After deposition of the first 5 Å of Al, all normal modes of pyridine are retained in the spectrum but show a slight decrease in absolute intensity. Upon additional deposition of Al, only the most intense bands for neat pyridine can still be distinguished, while the weaker bands at 383, 415, 709, 759, and 969 cm^{-1} become increasingly hard to discern. In addition, two broad and intense bands centered at 1287 and 1527 cm^{-1} grow in and dominate the spectra along with a weaker broad band centered at 902 cm^{-1}.

As discussed above for the reaction of pyridine with Mg, these new broad bands are attributed to the formation of hydrogenated amorphous carbon (a-C:H). This assignment is substantiated by the presence of the bands at 1287, 1527, and 902 cm^{-1}, previously attributed to the D-, G-, and T-bands of this material.[79] The G-band is due to stretching vibrations of sp^2-hybridized C atoms in both rings and chains, while the D-band is due to the breathing of sp^2-hybridized C atoms in rings. The T-band is characteristic of the stretching vibrations of sp^3-hybridized C atoms.[50,79] It is well-documented that the peak intensities, frequencies, and fwhm values of these vibrational bands vary depending on the degree of order/disorder of the

Table 3. Raman Peak Frequencies and Assignments for a 5-L Solid-State Pyridine Film before and after Al Deposition

Frequency (cm^{-1})		pyridine assignments[a]		amorphous carbon assignments[b]
pristine film	post Al deposition	Wilson no.	assignments	mode designation
383		ν_{16a}	$\delta(\text{ring})_{oop}$	
415		ν_{16b}	$\delta(\text{ring})_{oop}$	
613	613	ν_{6a}	$\delta(\text{ring})_{ip}$	
658	658	ν_{6b}	$\delta(\text{ring})_{ip}$	
709		ν_{11}	$\delta(\text{C–H})_{oop}$	
759		ν_4	$\delta(\text{ring})_{oop}$	
	902			T-band
969		ν_{10b}	$\delta(\text{C–H})_{oop}$	
998	998	ν_1	sym ring breathing (ip)	
1039	1039	ν_{12}	trig ring breathing (ip)	
1065	1065	ν_{18a}	$\delta(\text{C–H})_{ip}$	
1150	1160	ν_{15}		
1210	1210	ν_{9a}	$\nu(\text{ring})_{ip}$	
1228	1228	ν_3	$\delta(\text{C–H})_{ip}$	
	1287			D-band
1367	1367	ν_3	$\delta(\text{C–H})_{ip}$	
1487	1508	ν_{19a}	$\delta(\text{C–H})_{ip}$	
	1527			G-band
1579	1579	ν_{8b}	$\nu(\text{ring})_{ip}$	
1582	1582	ν_{8a}	$\nu(\text{ring})_{ip}$	
1602	1621	$\nu_1 + \nu_{6a}$		

[a]Assignments taken from ref 54. [b]Assignments taken from refs 50 and 79.

dx.doi.org/10.1021/jp300795c | J. Phys. Chem. C 2012, 116, 11548−11555

carbon forms, ranging from highly ordered forms (e.g., graphite) down to completely amorphous forms.[50] An estimate of the degree of order can be ascertained from the value of the intensity ratio $I(D)/I(G)$. For the spectra presented in Figure 7, this ratio is 0.43, which, along with the G peak frequency of 1527 cm^{-1}, is indicative of polymeric amorphous carbon.[50,79]

Further evidence for the consumptive reaction chemistry proposed can be seen in the plot of normalized intensities as a function of Al coverage in Figure 8. This plot clearly shows the

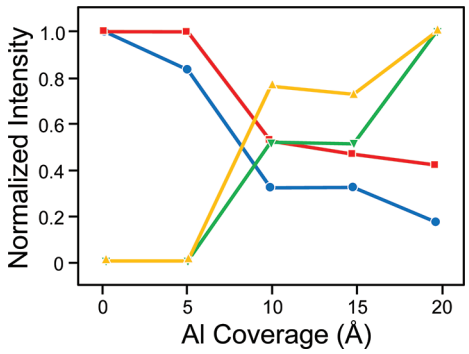

Figure 8. Normalized Raman intensities as a function of Al coverage for the unreacted pyridine bands at 658 cm^{-1} (blue ●) and 998 cm^{-1} (red ■) and for amorphous carbon at 1287 cm^{-1} (green ▼) and 1527 cm^{-1} (yellow ▲).

growth of the amorphous carbon bands at 1287 and 1527 cm^{-1} at the expense of the neat pyridine bands at 658 and 998 cm^{-1}. Moreover, although some evidence for a small amount of amorphous carbon was observed as a minor product in the reaction of pyridine with Mg, it appears to be the only product in the reaction of pyridine with post-deposited Al. This carbonization process is proposed to be initiated by formation of the anion radical, similar to the first step in the scheme in Figure 4 for the reaction between pyridine with Mg. As noted above, theoretical studies of pyridyl radical decomposition[78,61] indicate that pyridyl radicals can undergo ring-opening with further decomposition. On the basis of the observed spectra, these processes appear to proceed too rapidly to observe any of the radical intermediates.

The significant difference in the reaction of pyridine with Mg versus Al is likely due to stabilization of the *p*-pyridyl radical anion by weak coordination of Mg^+ through the N lone pair electrons leading to dimerization. No evidence exists for a similar coordination of Al cations.[65] Thus, the pyridyl radical anion must immediately degrade through a ring-opening process leading to decomposition.[61,78]

One final aspect of the reaction between solid-state pyridine and post-deposited Al deserves comment. If the reaction pathway leads to formation of amorphous carbon as proposed, this leaves the fate of the remaining N to be defined. One possible fate for the residual N could be its incorporation into the amorphous carbon film as some form of a nitrogen dopant. Unfortunately, elucidating definitive spectral evidence for this hypothesis is difficult given the small amount likely to be present. Moreover, significant spectral overlap between C═C and C═N stretching modes of these two amorphous materials is likely, making them spectrally indistinguishable,[51,80] although positive spectral identification of nitrogen-doped amorphous carbon might be possible through UV excitation in which the sp^1 bonds would be resonantly enhanced.[51]

CONCLUSIONS

Deposition of Mg onto pyridine films shows chemically specific reactivity induced by the transfer of an electron to pyridine, producing a pyridyl radical anion that is stabilized by weak coordination of Mg^+ by the pyridyl N. Although the spectral evidence suggests a weak chemisorptive interaction of pyridine with Ag, there is no evidence for pyridyl radical anion production by complete electron transfer. This is presumably due to the more covalent nature of the interaction between the pyridine N p_z and Ag d_z^2 orbitals. Stabilization of the Mg^+–pyridyl radical anion pair allows dimerization of these species to form 4,4′-bipyridine.

In contrast, even though electron transfer from Al to pyridine is more favorable than from Mg to pyridine due to its lower ionization potential (5.98 eV for Al[81] compared to 7.66 eV for Mg[81]), there is no evidence for stabilization of the radical anion by Al through metal-N coordination, and thus, the radical anion rapidly decomposes to amorphous carbon.

The findings reported here provide insight into the complex reaction chemistry possible between solid-state aromatic heterocyclic systems and reactive metal atoms. In comparing these results to those previously reported for analogous solid-state thin films of benzene by Schalnat,[26] it is noted that a higher degree of reactivity is observed upon introduction of the N heteroatom of pyridine due to the greater electron affinity of the aromatic heterocylic ring compared to the benzene aromatic ring. In instances where low work function metals (e.g., Mg, Al, and Ag) are deposited onto organic thin films containing heteroatoms, substantial reaction chemistry is clearly possible. This chemistry has significant ramifications for the performance of organic electronic devices wherein device performance is ultimately dictated by the molecular details of the interface.

AUTHOR INFORMATION

Corresponding Author

*E-mail: pembertn@u.arizona.edu.

Notes

The authors declare no competing financial interest.

ACKNOWLEDGMENTS

These studies were supported as part of the Center for Interface Science: Solar Electric Materials, an Energy Frontier Research Center funded by the U.S. Department of Energy, Office of Science, Office of Basic Energy Sciences, under award number DE-SC0001084. The instrumentation for this work was supported by the National Science Foundation through grant awards CHE-0317114 and CHE-0848624.

REFERENCES

(1) Fonseca, J. d. S. L.; Junior, A. d. C. F.; Grau, J. M.; Rangel, M. d. C. *Appl. Catal., A* **2010**, *386*, 201.
(2) Ashmore, J.; Green, J. C.; Green, M. L. H.; Smith, M. L.; Mehnert, C.; Wucherer, E. J. *J. Chem. Soc., Dalton Trans.* **1995**, 1873.
(3) Pradeep, K. S.; Vinod, K. S. *Pure Appl. Chem.* **2010**, *82*, 1845.
(4) Stockigt, D. *Organometallics* **1999**, *18*, 1050.
(5) Jiann, K.-T.; Presley, B. J. *Anal. Chem.* **2002**, *74*, 4716.
(6) Johnson, F. M. *Spectrochim. Acta, Part A* **2006**, *65*, 1154.
(7) Brody, F.; Ruby, P. R. *Heterocyclic Compounds, Pyridine and Derivatives*; Interscince Publishers: New York, 1960; Vol. *1*.
(8) Coutts, R. T.; Casy, A. F. *Pyridine and Its Derivatives*; John Wiley & Sons: New York, 1975; Vol. Part *4*.

(9) Gilchrist, T. L. *Heterocyclic Chemistry*, 3rd ed.; Singapore Publisher Inc.: Singapore, 1997.
(10) Rodgers, M. T.; Armentrout, P. B. *Acc. Chem. Res.* **2004**, *37*, 989.
(11) Rodgers, M. T.; Stanley, J. R.; Amunugama, R. *J. Am. Chem. Soc.* **2000**, *122*, 10969.
(12) Apps, D. K. *Biochim. Biophys. Acta* **1973**, *320*, 379.
(13) Liu, H.-C.; Zhang, X.-H.; Wang, C.; Wu, Y.-D.; Yang, S. *Phys. Chem. Chem. Phys.* **2007**, *9*, 607.
(14) Liu, X.-J.; Hamilton, I. P.; Han, K.-L.; Tang, Z.-C. *Phys. Chem. Chem. Phys.* **2010**, *12*, 10602.
(15) Walker, N.; Dobson, M. P.; Wright, R. R.; Barran, P. E.; Murrell, J. N.; Stace, A. J. *J. Am. Chem. Soc.* **2000**, *122*, 11138.
(16) Yang, Y.-S.; Hsu, W.-Y.; Lee, H.-F.; Huang, Y.-C.; Yeh, C.-S.; Hu, C.-H. *J. Phys. Chem. A* **1999**, *103*, 11287.
(17) Yang, Y.-S.; Yeh, C.-S. *Chem. Phys. Lett.* **1999**, *305*, 395.
(18) Guo, W.; Liu, H.; Yang, S. *Int. J. Mass Spectrom.* **2003**, *226*, 291.
(19) Guo, C.; Cao, Z.; Zhang, Q. *Chem. Phys. Lett.* **2004**, *386*, 448.
(20) Stangret, J.; Savoie, R. *J. Mol. Struct.* **1993**, *297*, 91.
(21) Hahn, J. R.; Kang, H. S. *Surf. Sci.* **2010**, *604*, 258.
(22) Sun, M.; Wan, S.; Liu, Y.; Jia, Y.; Xu, H. *J. Raman Spectrosc.* **2008**, *39*, 402.
(23) Wu, D.-Y.; Ren, B.; Jiang, Y.-X.; Xu, X.; Tian, Z.-Q. *J. Phys. Chem. A* **2002**, *106*, 9042.
(24) Adams, C. J.; Haddow, M. F.; Hughes, R. J. I.; Kurawa, M. A.; Orpen, A. G. *Dalton Trans.* **2010**, *39*, 3714.
(25) Marzec, K. M.; Gawel, B.; Lasocha, W.; Proniewicz, L. M.; Malek, K. *J. Raman Spectrosc.* **2010**, *41*, 543.
(26) Schalnat, M. C.; Hawkridge, A. M.; Pemberton, J. E. *J. Phys. Chem. C* **2011**, *115*, 13717.
(27) Arenas, J. F.; Lopez Tocon, I.; Otero, J. C.; Marcos, J. I. *J. Phys. Chem.* **1996**, *100*, 9254.
(28) Fleischmann, M.; Hendra, P. J.; McQuillan, A. J. *Chem. Phys. Lett.* **1974**, *26*, 163.
(29) Wetzel, H.; Gerischer, H.; Pettinger, B. *Chem. Phys. Lett.* **1981**, *78*, 392.
(30) Yamada, H.; Yamamoto, Y. *Surf. Sci.* **1983**, *134*, 71.
(31) Yamada, H.; Nagata, H.; Toba, K.; Nakao, Y. *Surf. Sci.* **1987**, *182*, 269.
(32) Moskovits, M.; DiLella, D. P.; Maynard, K. J. *Langmuir* **1988**, *4*, 67.
(33) Rowe, J. E.; Shank, C. V.; Zwemer, D. A.; Murray, C. A. *Phys. Rev. Lett.* **1980**, *44*, 1770.
(34) Muniz-Miranda, M.; Cardini, G.; Schettino, V. *Theor. Chem. Acc.* **2004**, *111*, 264.
(35) Mendoza, O.; Tacke, M. *J. Organomet. Chem.* **2006**, *691*, 1110.
(36) Shvartsburg, A. A. *Chem. Phys. Lett.* **2003**, *376*, 6.
(37) Heimel, G.; Romaner, L.; Zojer, E.; Brédas, J.-L. *Nano Lett.* **2007**, *7*, 932.
(38) Ishii, H.; Sugiyama, K.; Ito, E.; Seki, K. *Adv. Mater.* **1999**, *11*, 605.
(39) Shen, C.; Kahn, A.; Schwartz, J. *J. Appl. Phys.* **2001**, *89*, 449.
(40) Stossel, M.; Staudigel, J.; Steuber, F.; Simmerer, J.; Winnacker, A. *Appl. Phys. A* **1999**, *68*, 387.
(41) Oyamada, T.; C., M.; Sasabe, H.; Adachi, C. *Jpn. J. Appl. Phys.* **2003**, *42*, L1535.
(42) Davis, R. J.; Pemberton, J. E. *J. Phys. Chem. C* **2008**, *112*, 4364.
(43) Davis, R. J.; Pemberton, J. E. *J. Am. Chem. Soc.* **2009**, *131*, 10009.
(44) Hawkridge, A. M.; Pemberton, J. E. *J. Am. Chem. Soc.* **2002**, *125*, 624.
(45) Taylor, C. E.; Garvey, S. D.; Pemberton, J. E. *Anal. Chem.* **1996**, *68*, 2401.
(46) Tiani, D. J.; Pemberton, J. E. *Langmuir* **2003**, *19*, 6422.
(47) Smolinski, S.; Zelenay, P.; Sobkowski, J. *J. Electroanal. Chem.* **1998**, *442*, 41.
(48) Goodman, D. W.; Madey, T. E.; Ono, M.; Yates, J. T. *J. Catal.* **1977**, 279.
(49) Adamson, A. W. *Physical Chemistry of Surfaces*, 5th ed.; John Wiley & Sons, Inc.: New York, 1990.
(50) Ferrari, A. C.; Robertson, J. *Phys. Rev. B* **2000**, *61*, 14095.
(51) Benassi, R.; Ferrarini, P.; Fontanesi, C.; Benedetti, L.; Paolucci, F. *J. Electroanal. Chem.* **2004**, *564*, 231.
(52) Dodd, J. G.; DeNoyer, L. K. Curve-Fitting: Modeling Spectra. *Handbook of Vibrational Spectroscopy*; Wiley Ineterscience: New York, 2002; p 1919.
(53) Creighton, J. A. *Surf. Sci.* **1986**, *173*, 665.
(54) Vivoni, A.; Birke, R. L.; Foucault, R.; Lombardi, J. R. *J. Phys. Chem. B* **2003**, *107*, 5547.
(55) Gao, P.; Weaver, M. J. *J. Phys. Chem.* **1985**, *89*, 5040.
(56) Zhao; Jensen, L.; Schatz, G. C. *J. Am. Chem. Soc.* **2006**, *128*, 2911.
(57) Pettinger, B. *Chem. Phys. Lett.* **1981**, *78*, 404.
(58) Goncher, G. M.; Parsons, C. A.; Harris, C. B. *J. Phys. Chem.* **1984**, *88*, 4200.
(59) Salvan, G.; Zahn, D. R. T.; Paez, B. *J. Luminesc.* **2004**, *110*, 296.
(60) Zahn, D. R. T.; Gavrila, G. N.; G., S. *Chem. Rev.* **2007**, *107*, 1161.
(61) Cheng, X. L.; Zhao, Y. Y.; Zhou, Z. Y. *J. Mol. Struct.: THEOCHEM* **2004**, *678*, 17.
(62) LaVerne, J. A.; Carmichael, I.; Araos, M. S. *J. Phys. Chem. A* **2005**, *109*, 461.
(63) Nenner, I.; Schulz, G. J. *J. Chem. Phys.* **1975**, *62*, 1747.
(64) Han, S. Y.; Song, J. K.; Kim, J. H.; Oh, H. B.; Kim, S. K. *J. Chem. Phys.* **1999**, *111*, 4041.
(65) Chaudhuri, J.; Kume, S.; Jagur-Grodzinski, J.; Szwarc, M. *J. Am. Chem. Soc.* **1968**, *90*, 6421.
(66) Newkome, G. R.; Hager, D. C. *J. Org. Chem.* **1982**, *47*, 599.
(67) Schmulbach, C. D.; Hinckley, C. C.; Wasmund, D. *J. Am. Chem. Soc.* **1968**, *90*, 6600.
(68) Joule, J. A.; Mills, K. *Heterocyclic Chemistry*, 4th ed.; Blackwell Science: Malden, MA, 2000.
(69) Topaçli, A.; Akyüz, S. *Spectrochim. Acta, Part A* **1995**, *51*, 633.
(70) Castellà-Ventura, M.; Kassab, E. *J. Raman Spectrosc.* **1998**, *29*, 511.
(71) Zhuang, Z.; Ruan, W.; Ji, N.; Shang, X.; Wang, X.; Zhao, B. *Vib. Spectrosc.* **2009**, *49*, 118.
(72) Gu, R.-a.; Shen, X.-y.; Cui, Y.; Gu, W. *Spectrosc. Spect. Anal.* **2006**, *26*, 452.
(73) Joo, S.-W. *Vib. Spectrosc.* **2004**, *34*, 269.
(74) Lim, J. K.; Joo, S.-W. *Surf. Interface Anal.* **2007**, *39*, 684.
(75) Lu, T.; Cotton, T. M.; Birke, R. L.; Lombardi, J. R. *Langmuir* **1989**, *5*, 406.
(76) Strekas, T. C.; Diamandopoulos, P. S. *J. Phys. Chem.* **1990**, *94*, 1986.
(77) Santisteban, J. R.; Cuello, G. J.; Dawidowski, J.; Fainstein, A.; Peretti, H. A.; Ivanov, A.; Bermejo, F. J. *Phys. Rev. B* **2000**, *62*, 37.
(78) Liu, R.; Huang, T. T. S.; Tittle, J.; Xia, D. *J. Phys. Chem. A* **2000**, *104*, 8368.
(79) Casiraghi, C.; Ferrari, A. C.; Robertson, J. *Phys. Rev. B* **2005**, *72*, 085401.
(80) Niu, L.; Zhu, J.; Gao, W.; Han, X.; Du, S. *Chin. Sci. Bull.* **2009**, *54*, 4376.
(81) *Handbook of Chemistry and Physics*, 87th ed.; CRC Press: Boca Raton, FL, 2006.
(82) Kihara, H.; Gondo, Y. *J. Raman Spectrosc.* **1986**, *17*, 263.
(83) He, Y.; Liu, Y.; Zhao, Y. *Nanotechnology* **2008**, *19*, 465602.